

Single- and Two-Component GRB Spectra in the Fermi GBM-LAT Energy Range

P. Veres and P. Mészáros

*Dept. of Astronomy & Astrophysics, Dept. of Physics and Center for Particle
Astrophysics, 525 Davey Lab., Pennsylvania State University, University Park,
PA 16802, USA*

veresp@psu.edu, nnp@astro.psu.edu

ABSTRACT

Most Fermi GRB spectra appear as either a broken power law extending to GeV energies or as a broken power with a separate GeV power law component. Here we show that such spectra can be understood in terms of magnetically dominated relativistic jets where a dissipative photosphere produces the prompt MeV emission, which is extended into the GeV range by inverse Compton scattering in the external shock, with possible contributions from a reverse shock as well. The bulk Lorentz factors required in these models are in the range of 300-600, and the MeV-GeV time delays arise naturally. In some cases an optical flash and a sub-dominant thermal component are also present.

1. Introduction

The GRB spectra observed with the *LAT* detector on *Fermi* reveal a diversity of appearances. Some have spectra consistent with a single canonical Band function (Band et al. 1993) extending to the highest detected multi-GeV energies, while in others at the higher end of the Band spectrum a second, flatter spectral component emerges, which sometimes appears to have a cutoff (Pelassa 2011; Pe'er 2011). The origin of such a dichotomy, as well as the extent of the applicability of such spectra for deriving lower limits on the bulk Lorentz factor (Kocevski & The Fermi Collaboration 2012) are the subject of ongoing research and discussions.

Here we investigate possible scenarios for these two spectral types in the context of magnetically dominated, baryon loaded outflows, where the prompt MeV

emission arises in the jet photosphere. Magnetically dominated models have recently received increased attention (Drenkhahn & Spruit 2002; Lyutikov & Blandford 2003; Giannios & Spruit 2007; Giannios 2012; Komissarov et al. 2009; McKinney & Uzdensky 2011; Metzger et al. 2011a; Mészáros & Rees 2011; Bošnjak & Kumar 2012; Zhang & Yan 2011), while photospheric emission, either in baryonic or magnetic models where dissipation occurs near the photosphere, have been shown to be able to produce Band-like non-thermal spectra (Pe’er et al. 2006; Lazzati et al. 2011; Beloborodov 2010; Ryde et al. 2010; Pe’er et al. 2012). In the scenarios that we discuss here we combine these two elements and add a third one, assuming that the prompt spectrum is a combination of the emission from two distinct regions, namely, a magnetically dominated dissipative photosphere and the external shock. We argue that the photosphere is initially responsible for the low energy (*GBM*) part of the Band-like prompt spectrum, the final observed spectrum being modified by inverse Compton scattering in the external shock, which results in a delayed high energy (*LAT*) component. The latter includes a forward and possibly also a reverse shock contribution, dominated by self-inverse Compton (SSC) as well as external inverse Compton (EIC) of the photospheric photons. We consider here mainly the radial structure of the outflow, and restrict ourselves to leptonic mechanisms.

Our primary goal here is to explore the generic features of such models, and to test the extent to which they qualitatively lend themselves to the interpretation of *LAT* spectra. That is, we do not perform detailed fits to individual bursts, which at this point would be premature given the preliminary nature and the uncertainties in the models. The purpose is to explore the connection between elements of the physical model and the presence or absence of broad spectral features, and how these depend on typical burst parameters. We concentrate on the prompt emission, from the time of the trigger up to times comparable to the deceleration time, when the external forward shock (and the reverse, if present) have fully developed. The latter should be representative of the physics in the late afterglow, which we do not address specifically here. We then qualitatively compare our results to several of the archetypal *LAT* bursts, such as GRB 090902B (Abdo & the Fermi collaboration 2009), which has a Band component and an extra high energy power law (PL) second component; GRB 090926, which also has an extra spectral component and shows a high energy cutoff (Ackermann & the Fermi collaboration 2011); and GRB 080916C, which shows a single Band component extending to multi-GeV (Abdo et al. 2009).

We show that in the context of these models, this variety of appearances can be attributed to differences in the strength of the various radiation components under plausible variations of the input physical parameters. Previous investigations (e.g., Toma et al. 2011b; Fraija et al. 2012) have considered a connection between the extra high energy component and inverse Compton and/or a reverse shock in a baryon dominated outflow. Here the magnetically dominated dynamics, photospheric input spectrum and consideration of separate SSC and EIC components from both forward and reverse shock result in a different and broader range of possible outcomes. Depending on the parameters, the SSC or EIC from the forward shock and the reverse shock (if the latter is present) can either result in an extra high energy component, or sometimes in an apparent single Band component extending to the highest energies. We show that, even if there is a pair-production cutoff in the nonthermal prompt emission at a few or a few tens of MeV, the external inverse Compton radiation from the reverse shock can constitute a natural extension of the absorbed emission to form a continuous Band spectrum out to higher energies. We argue that if a reverse shock does not develop, the dominant high-energy components will be the forward shock SSC or EIC, resulting in a distinct extra component. For some parameters, however, the latter can also be produced by a reverse shock. A further result from these calculations is that, since the high energy component arises mainly in the external shock, where the compactness parameter is low, these high energy photons do not constrain via $\gamma\gamma$ cutoff considerations the bulk Lorentz factor to as high values as considered in many of the recent analysis papers.

In §2 we discuss the basic magnetic jet model used. In §3 we give the details of the dissipative photospheric (prompt) spectrum. In §4 we discuss the various external shock synchrotron and inverse Compton radiation components. In §5 we present numerical results for various cases. In §6 we discuss our results and conclusions.

2. Magnetic Model

We assume a total luminosity $L_t = 10^{53} L_{t,53}$ erg/s is released at a radius $r_0 = 10^7 r_{0,7}$ cm, lasting for 10 s in the central engine frame. This is initially (at r_0) mainly magnetic, which at larger radii gets gradually converted into bulk kinetic energy and non-thermal radiation. We assume that at the dissipative photosphere

a fraction ζ_r of L_t is released as prompt radiation, whose spectrum is discussed in the next section. A nominal value for this here is $\zeta_r \simeq 0.5$, which we assume to consist mainly of a non-thermal component $\zeta_{nt} \sim \zeta_r$ giving the Band power law (PL) spectrum (a smaller fraction of ζ_r is in a thermal component $\zeta_{th} < \zeta_{nt}$, discussed in §3.2, so that $\zeta_r = \zeta_{nt} + \zeta_{th}$). The remaining energy fraction beyond the photosphere ζ_k , after the Lorentz factor reaches its saturation (coasting) value, is in kinetic energy form. About half of this, $\zeta_d \simeq 0.25$, is assumed to be radiated away in the external shock (forward and reverse) when deceleration starts, while the other half, $\zeta_{ag} \simeq 0.25$, continues as kinetic energy of the decelerating ejecta, and is eventually radiated away in the longer afterglow phase. Thus, $\zeta_r + \zeta_k = 1$. Most of our results are evaluated for $\zeta_r = 1 - \zeta_k = 0.5$, and we use these nominal numerical fractions unless stated otherwise. These factors are used to define the respective luminosities, e.g., $L_{k,53} = (1 - \zeta_r)L_{t,53}$, etc., and we use the $Q = 10^x Q_x$ convention in cgs units, except, e.g. for the coasting Lorentz factor ($\eta = 600 \eta_{600}$).

We consider a continuous outflow in which the central engine is active for $t_{0,\text{obs}} = 20 t_{1.3}(1+z)/2$ s, while the deceleration time is \sim few seconds resulting in a modestly thick-shell deceleration region, which for simplicity will be approximated as a thin shell. We assume a constant density external medium ($n = 1 n_0 \text{ cm}^{-3}$) and a burst with a fiducial redshift and luminosity distance of $z = 1$ or $D_L = 2 \times 10^{28} D_{28.3} \text{ cm}$.

In magnetically dominated models the magnetic fields become rapidly transverse, in a striped magnetic structure (Kennel & Coroniti 1984). The Lorentz factor in such jets will increase more slowly than in a matter dominated case, e.g. after a few characteristic lengths above r_0 the average Lorentz factor will increase as r^m , where m depends on the geometry assumed at the lower boundary (e.g., McKinney & Uzdensky 2011; Narayan et al. 2010). When magnetic reconnection plays a role, the expected Lorentz factor behavior is $\gamma \propto r^{1/3}$ until it saturates (Drenkhahn 2002; Giannios & Spruit 2007; Metzger et al. 2011b; Mészáros & Rees 2011), which we assume in what follows.

$$\Gamma(r) \propto \begin{cases} r^{1/3} & \text{if } r < r_{sat} \\ \text{const.} & \text{if } r_{sat} < r < r_{dec}, \end{cases} \quad (1)$$

where r_{sat} is the saturation radius where $\Gamma \rightarrow \eta \equiv L_t/\dot{M}c^2$ and $r_{dec} > r_{sat}$ is the deceleration radius. We will concern ourselves here only with the behavior before and in the neighborhood of the deceleration radius, and do not consider

the longer term afterglow phase. A feature worth stressing is that an acceleration behavior such as equ. (1) implies a comoving volume element $V' \propto r^2 \Gamma(r)$ scaling leading to a radius dependence of the comoving particle density n' , temperature T' , etc. which differs from that in the usual baryon-dominated $\gamma \propto r$. Also, the saturation radius occurs at significantly larger radii than in the matter dominated acceleration cases, if other relevant quantities are the same. Furthermore, the scattering photospheric radius (see equ. [2]) occurs generally before the saturation radius.

3. Prompt Photospheric Radiation

The photospheric radius is obtained by setting the scattering optical depth to unity for the ejecta, i.e. $\tau_T = L_r / (4\pi r^2 m_p c^3 \eta \Gamma) \sigma_T r / (2\Gamma) = 1$, if the e^+e^- pair contribution can be ignored. The effect of pairs will be that they will increase the photospheric radius. With the increased radius variables have to be recomputed, resulting in a different cutoff energy and in a different number of pairs. At the end of this iterative process, we find that the photospheric radius increases by a factor of ~ 5 for the nominal parameters (see also Bošnjak & Kumar 2012). We address the details of pair creation at the end of this section.

For $\Gamma = (r/r_0)^{1/3}$ the photospheric radius at which $\tau_T = 1$ is

$$r_{ph} = \left(\frac{L_r r_0^{2/3} \sigma_T}{8\pi m_p c^3 \eta} \right)^{3/5} = 6.5 \times 10^{12} L_{t,53}^{3/5} \zeta_r^{3/5} r_{0,7}^{2/5} \eta_{600}^{-3/5} \text{ cm} \quad (2)$$

for a nominal $\eta = 600$, where σ_T is the Thomson cross section. The photospheric radius occurs in the accelerating phase for any realistic set of parameters, for the magnetized dynamics described in the previous section. The saturation radius, where the acceleration ceases and the ejecta starts to coast with $\Gamma \sim \eta \simeq \text{constant}$ is, for a magnetically dominated jet, at

$$r_{sat} = r_0 \eta^3 = 2.2 \times 10^{15} r_{0,7} \eta_{600}^3 \text{ cm.} \quad (3)$$

While compared to baryonic outflow models the photosphere is relatively farther away from the central engine, both the photosphere and the saturation radius remain generally smaller than the deceleration radius,

$$r_{dec} = \left(\frac{3L_k t_0}{4\pi n m_p c^2 \Gamma^2} \right)^{1/3} = 4.8 \times 10^{16} L_{t,53}^{1/3} (1 - \zeta_r)^{1/3} t_{1.3}^{1/3} n_0^{-1/3} \eta_{600}^{-2/3} \text{ cm.} \quad (4)$$

This is the radius at which we calculate, in §4, the interaction of the photospheric photons with the external shock electrons, resulting in SSC and EIC components. Using the scaling relations of the magnetic dynamics, the density decreases with radius as $n'_b \propto V'^{-1} \propto r^{-7/3}$ for $r < r_{sat} = r_0 \eta^3$ and $n'_b \propto r^{-2}$ for $r_{sat} < r$, that is, $n'_b(r) = n'_0 (r/r_0)^{-7/3}$ for $r < r_{sat}$ and $n'_b(r) = n'_{sat} (r/r_{sat})^{-2}$ for $r_{sat} < r$. Thus, the comoving baryon density at the deceleration radius is $n'_{b,dec} = 5.3 \times 10^4 (1 - \zeta_r)^{-2/3} L_{t,53}^{1/3} \eta_{600}^{-2/3} n_0^{2/3} t_{1.3}^{-2/3} \text{ cm}^{-3}$.

3.1. Nonthermal Photospheric Spectrum

Near the scattering photosphere, a prompt spectrum with a high radiation efficiency can be produced through dissipative effects. For non-magnetic outflows, such photospheres were considered by, e.g. Rees & Mészáros (2005); Pe’er et al. (2006); Beloborodov (2010), while for magnetic photospheres dissipation of magnetic energy via reconnection, turbulence dissipation or the associated semi-relativistic shocks was considered by, e.g. Giannios & Spruit (2007); Giannios (2012); McKinney & Uzdensky (2011); Mészáros & Rees (2011). This generally can convert some fraction ζ_r of the initial jet energy L_t into a prompt burst of radiation, the rest remaining available as kinetic energy of the coasting ejecta beyond the saturation radius. The spectrum of an unmagnetized dissipative outflow in the photospheric neighborhood has been calculated by Beloborodov (2010), who performed a radiative transfer calculation including both thermal and non-thermal electrons from nuclear collisions which results in a Band spectrum with spectral indices in the range of those observed (see also Vurm et al. (2011) for inclusion of magnetic fields up to $\epsilon_B \sim 1$). Magnetic photospheres where reconnection leads to magnetic turbulence and/or dissipation combined with Comptonization effects involving purely thermal electrons were calculated by Thompson (1994) and Giannios & Spruit (2007), resulting also in Band-like spectra with spectral slopes close to the average observed values $\alpha = 1$ and $\beta = 2$. Of course, the dissipation of energy can occur in magnetic cases both below and above the photosphere, up to the saturation radius (Giannios 2008), and also in non-magnetic cases scattering occurring both below and for some distance above the photosphere can affect the spectrum (Pe’er et al. 2006; Beloborodov 2010). These calculations indicate that the spectral peak occurs naturally in the neighborhood of $\varepsilon_{pk} \sim 300 \text{ keV}$. Dissipation radii larger than the photosphere would permit also multi-GeV prompt photons to escape if these are indeed produced as shown by Giannios (2008); Be-

Beloborodov (2010); Vurm et al. (2011).

Here we do not specialize to a specific dissipation mechanism, and we consider an idealized photospheric model where some fraction $\zeta_r \sim 0.5$ of the initial outflow luminosity is converted into prompt radiation near the nominal radius r_{ph} of the photosphere, producing a Band-like spectrum whose slopes are in the range of the observed values. In order to connect this spectrum to the magnetic properties of the flow, we assume that the spectral peak is given by the synchrotron spectral peak of the minimum energy electrons accelerated in the dissipative photosphere, which as it happens turns out also to be in the observed range of ~ 300 keV. (Note that, in principle, the prompt emission model could also be taken to be a nonmagnetic photosphere, as in Pe’er et al. (2006); Beloborodov (2010); the photospheric radius would be different, but the upscattering in the external shock would differ only insofar as caused by any possible differences in the photospheric seed spectrum. Also, the range of radii over which the prompt spectrum forms does not have an impact on the upscattered spectrum, as long as the external shock lies significantly beyond the dissipation and saturation radii).

The value of the Lorentz factor at the magnetic photosphere is

$$\Gamma_{ph} = (r_{ph}/r_0)^{1/3} = 87 L_{t,53}^{1/5} \zeta_r^{1/5} r_{0,7}^{-1/5} \eta_{600}^{-1/5}. \quad (5)$$

At this photosphere, the magnetic dissipation and/or collisional effects such as n, p decoupling will lead to a significant non-thermal electron component. E.g. for reconnection acceleration or semi-relativistic shocks associated with reconnection (Mészáros & Rees 2011), a typical minimum comoving electron random Lorentz factor $\gamma_{e,ph} \sim 600\Gamma_r$, coincidentally of similar order of magnitude as η . The magnetic field at the photosphere is $B'_{ph} = (32\pi\epsilon_B m_p c^2 n'_b)^{1/2} \Gamma_r = 1.7 \times 10^6 L_{t,53}^{-1/5} (1 - \zeta_r)^{1/2} \zeta_r^{-7/10} r_{0,7}^{-3/10} \eta_{600}^{1/5} \epsilon_{B,0}^{1/2} \Gamma_r$ G. Here n'_b is the comoving baryon density evaluated at the photosphere, $n'_{b,ph} = L_k / (4\pi m_p c^3 r_{ph}^2 \eta \Gamma_{ph}) = 2.0 \times 10^{13} L_{t,53}^{-2/5} \zeta_r^{-7/5} (1 - \zeta_r) r_{0,7}^{-3/5} \eta_{600}^{2/5} \text{ cm}^{-3}$, Here as before, L_k and L_r are expressed as functions of L_t and ζ_r . The observed synchrotron spectral peak of the photosphere will be

$$\varepsilon_{sy}^{ph,obs} = \varepsilon_{br} = \frac{3ehB'_{ph}}{4\pi m_e c} \gamma_{e,ph}^2 \frac{\Gamma_{ph}}{1+z} = 310 \zeta_r^{-1/2} (1 - \zeta_r)^{1/2} r_{0,7}^{1/2} \epsilon_{B,0}^{1/2} \Gamma_r^3 \left(\frac{1+z}{2} \right)^{-1} \text{ keV}, \quad (6)$$

corresponding to the Band peak. The magnetic field energy fraction at the photosphere is still $\epsilon_B \sim 1$, but dissipation will lead to values $\epsilon_{B,FS} \lesssim 0.1$ by the time the flow reaches the deceleration radius. Following Thompson (1994); Giannios

& Spruit (2007) and Beloborodov (2010), we assume that the emergent spectral shape is of the Band form, taking for its peak value dependence on the flow parameters the expression (6). As a nominal photon number low energy spectral index we take $\alpha \simeq 1$ (where $N_\varepsilon(\varepsilon) \propto \varepsilon^{-\alpha}$) and for the high energy spectral index $\beta \simeq 2.4$. The flux in energy per energy units is then

$$F_\varepsilon = A \begin{cases} \left(\frac{\varepsilon}{\varepsilon_{br}}\right)^{-\alpha+1} & \text{if } \varepsilon \leq \varepsilon_{br} \\ \left(\frac{\varepsilon}{\varepsilon_{br}}\right)^{-\beta+1} & \text{if } \varepsilon > \varepsilon_{br} \end{cases} \quad (7)$$

The flux is related to the luminosity via $L/4\pi D_L^2 = \int F_\varepsilon d\varepsilon$ which yields the normalization factor $A = L_r/(4\pi D_L^2 \varepsilon_{sy}^{ph,obs} (1/(2-\alpha) + 1/(\beta-2))) = 9.1 \times 10^{-9} L_{t,53} \zeta_r^{3/2} (1 - \zeta_r)^{-1/2} D_{L,28.3}^{-2} r_{0,7}^{1/2} \varepsilon_{B,0}^{-1/2} \Gamma_r^{-3} ((1+z)/2) \text{ erg cm}^{-2} \text{ s}^{-1} \text{ keV}^{-1}$. The $\varepsilon F_\varepsilon$ peak of the non-thermal spectrum will arise at ε_{br} and at $(\varepsilon F_\varepsilon)^{\max} = \varepsilon_{br} A = 2.8 \times 10^{-6} L_{t,53} \zeta_r D_{L,28.3}^{-2} \text{ erg cm}^{-2} \text{ s}^{-1}$. At low energies a self-absorption break is expected. In our case, this will occur at $\varepsilon_{SA} \approx 6.8 L_{t,53}^{1/5} \zeta_r^{-1/5} (1 - \zeta_r)^{1/5} \eta_{600}^{7/15} \varepsilon_{B,0}^{1/3} \text{ keV}$ (Guetta & Granot 2003a).

The high energy branch of the photospheric spectrum (7) extends up to an energy which is model dependent. We discuss here two scenarios. In the first scenario, photons above the photospheric spectral peak (6) are upscattered as a result of interactions with electrons associated with magnetic turbulent waves, up to an energy $\varepsilon' \approx m_e c^2$ in the jet frame (Thompson 1994). In our case, this corresponds to an observer frame cutoff at

$$\varepsilon_h \approx (4/3) m_e c^2 \Gamma_{ph} / (1+z) \approx 30 L_{t,53}^{1/5} \zeta_r^{-1/5} r_{0,7}^{-1/5} \eta_{600}^{-1/5} \left(\frac{1+z}{2}\right)^{-1} \text{ MeV}. \quad (8)$$

This corresponds to $\varepsilon' \sim m_e c^2$ in the comoving frame, and is below the $\gamma\gamma$ cutoff expected from pair production against photospheric lower energy photons (see below), so no pairs are created.

In the second scenario, we assume that the magnetic reconnection regions or the shocks associated with them are coherent over long enough times that electrons can be accelerated, e.g. via a Fermi mechanism, to a power law extending above the previous ε_h to photon energies sufficiently high to be subject to $\gamma\gamma$ interactions. We estimate the $\gamma\gamma$ annihilation energy from requiring the pair optical depth to be unity against target photons of energy ε_{at} .

$$\varepsilon_{\gamma\gamma} = (\Gamma_{ph} m_e c^2)^2 / [(1+z)^2 \varepsilon_{at}], \quad (9)$$

where $\tau_{\gamma\gamma} \sim 11/180 \sigma_T N_{>\varepsilon_{at}} / 4\pi r_{ph}^2$ (Lithwick & Sari 2001; Murase & Ioka 2008), where $N_{>\varepsilon}$ is the number of photons with energies higher than ε . This will result in

an observer-frame cut-off energy $\varepsilon_{\gamma\gamma} \sim 30 - 100$ MeV. If $\varepsilon_{\gamma\gamma} > \varepsilon_{at}$ is not satisfied, the cutoff will be at $\sim \Gamma_{ph} m_e c^2 / (1+z)$. Above the cut-off, the spectrum becomes steeper, the exact post cut-off spectral index depending on the spectrum and photon spatial distribution. A simple slab approximation, as discussed for GRB 090926A (Ackermann & the Fermi collaboration 2011), results in a steepening of the high energy slope index by $\beta - 1$ above the $\varepsilon_{\gamma\gamma}$ energy (see also Beloborodov 2010).

These pairs also radiate in the magnetic field of the prompt emission site, and this will result in a low energy synchrotron component peaking at tens of electron volts. As we discuss in §6, this component is a good candidate for the bright prompt optical emission observed in some bursts. The pair synchrotron component will be in the fast cooling regime, with $\gamma_{\pm,m} = \varepsilon_{\gamma\gamma}(1+z)/(2\Gamma_{ph}m_e c^2) = 3.9$ and $\varepsilon_{\pm,peak} \approx 3.2$ eV (e.g. Toma et al. 2011a). The functional dependence is different depending on the different cases for $\varepsilon_{\gamma\gamma}$. The peak of the $\varepsilon F_\varepsilon$ spectrum is 7.7×10^{-9} erg cm⁻² s⁻¹ for nominal parameters.

3.2. Thermal Component of the Photospheric Spectrum

In the presence of collisional or magnetic dissipation, in addition to a non-thermal component one expects also a thermal component, whose luminosity $L_{th} = \zeta_{th} L_t$ should have a quasi-blackbody spectrum. In our case, this peaks in the soft X-rays (Mészáros & Rees 2011), due to the different temperature scaling with radius for the magnetic dynamics, comprising a fraction ζ_{th} of the luminosity of the photosphere. This thermal component can be calculated from the initial $T_0 = \left(\frac{L_t}{4\pi r_0^2 a c \Gamma_r^2} \right)^{1/4} = 2.1 L_{t,53}^{1/4} r_{0,7}^{-1/2} \Gamma_r^{-1/2}$ MeV at the initial radius $r_0 = 10^7 r_{0,7}$ cm.

Above r_0 the magnetically dominated jet dynamics $\Gamma \propto r^{1/3}$ implies a comoving volume is $V' \propto r^2 \Gamma \propto r^{7/3}$ in the acceleration regime. Thus, the temperature will decrease more gradually with radius than in the baryon-dominated case (where $T' \propto r^{-1}$), as $T' \propto \rho'^{\hat{\gamma}-1} \propto \rho'^{1/3} \propto V'^{-1/3} \propto r^{-7/9}$, or $T'(r) = T_0 (r/r_0)^{-7/9}$, where $\hat{\gamma} = 4/3$ is the adiabatic exponent for a relativistic gas. Thus, at the photosphere $T(r_{ph}) = 2.7 L_{t,53}^{-1/60} \zeta_r^{-4/15} \eta_{600}^{4/15} r_{0,7}^{-7/30} \Gamma_r^{-1/2} \left(\frac{1+z}{2} \right)^{-1}$ keV.

The corresponding thermal luminosity is $L_{th} = 6.5 \times 10^{49}$ erg/s, which is low for producing the prompt emission, as well as being too soft. This blackbody component from the photosphere thus peaks in the soft X-rays at $(\varepsilon F_{\varepsilon,BB})^{peak} \approx$

$9.5 \times 10^{-9} L_{t,53}^{11/15} \zeta_r^{-4/15} \eta_{600}^{4/15} r_{0,7}^{4/15} \text{ erg cm}^{-2} \text{ s}^{-1}$. This thermal component is similar to the one found by Page et al. (2011).

4. External Shock Radiation Spectral Components

4.1. Forward Shock (FS) Synchrotron

The forward shock develops at the deceleration radius, where the jet has plowed up an amount of external mass roughly equal to $1/\eta$ times of the ejecta mass. The electrons in the shock will be accelerated into a relativistic energy distribution, and will undergo cooling through synchrotron emission and by inverse Compton scattering off external (photospheric) and their own (synchrotron) photons. At this deceleration radius the Lorentz factor has roughly halved from its coasting value. The time of the deceleration is $t_{dec} = r_{dec}/(2\eta^2 c)(1+z) \approx 4.4 L_{t,53}^{1/3} (1-\zeta_r)^{1/3} t_{1.3}^{1/3} n_0^{-1/3} \eta_{600}^{-8/3} (1+z)/2 \text{ s}$.

While at the photosphere the magnetic field parameter ϵ_B^{ph} is close to unity for a magnetically dominated model, after magnetic dissipation ceases one expects this parameter to be much less, the outflow becoming essentially baryon dominated (e.g., Zhang & Yan 2011). Here we assume that at the deceleration radius $\epsilon_B^{FS} \lesssim 0.1$.

The magnetic field in the forward shock is then $B'_{FS} = (32\pi m_p c^2 \epsilon_B \Gamma_{FS}^2 n)^{1/2} \approx 74 \eta_{600} \epsilon_{B,-1}^{1/2} n_0^{1/2} \text{ G}$. The cooling Lorentz factor is $\gamma_c = 6\pi m_e c / ((1+Y)\sigma_T B_{FS}^2 \Gamma t_{dec}) = 3/(8(1+Y)\sigma_T (m_p/m_e) \epsilon_B n r_{dec} \eta) = 98 (1-\zeta_r)^{-1/3} L_{t,53}^{-1/3} t_{1.3}^{-1/3} \epsilon_{B,-1}^{-1} n_0^{-2/3} \eta_{600}^{-1/3} (1+Y)^{-1}$, where $Y = (-1 + \sqrt{1 + 4\epsilon_e/\epsilon_{B,FS}})/2 \approx 0.1$ is the Compton parameter. The minimal (injection) Lorentz factor is

$$\gamma_m = \epsilon_e \frac{m_p p - 2}{m_e p - 1} \Gamma \equiv 3100 \epsilon_{e,-2} \eta_{600} g_{p,2.4}, \quad (10)$$

where $g_{p,2.4}$ is the fraction $(p-2)/(p-1)$ normalized to $p = 2.4$. Thus, the electrons responsible for the synchrotron radiation are in the fast cooling regime, and their distribution is given by $dN_e/d\gamma \propto \gamma^{-2}$ if $\gamma_c \leq \gamma < \gamma_m$ and $dN_e/d\gamma \propto \gamma^{-p-1}$ if $\gamma \geq \gamma_m$.

The observer frame energy of photons radiated by electrons with a random

Lorentz factor γ_m in the forward shock is

$$\varepsilon_m = \frac{3heB'_{FS}}{4\pi m_e c} \gamma_m^2 \frac{\Gamma_{FS}}{1+z} = 3.8 \epsilon_{B,-1}^{1/2} \epsilon_{e,-2}^2 n_0^{1/2} \eta_{600}^4 g_{p,2.4}^2 \left(\frac{1+z}{2}\right)^{-1} \text{ keV}, \quad (11)$$

while for electrons with a random Lorentz factor γ_c the observed photon energy is

$$\varepsilon_c = 3.7 L_{t,53}^{-2/3} (1 - \zeta_r)^{-2/3} t_{1.3}^{-2/3} \epsilon_{B,-1}^{-3/2} n_0^{-5/6} \eta_{600}^{4/3} (1+Y)^{-2} \left(\frac{1+z}{2}\right)^{-1} \text{ eV}. \quad (12)$$

The peak flux density of the FS synchrotron spectrum occurs, for fast cooling, at ε_c , and is given by (e.g. Sari et al. 1998):

$$F_{max}^{FS}(\varepsilon_c) = \frac{4\pi r_{dec}^3 n m_e c^2 \sigma_T \eta B'_{FS}}{3 \cdot 12\pi q_e D_L^2} = 0.15 L_{t,53} (1 - \zeta_r) t_{1.3} \epsilon_{B,-1}^{1/2} n_0^{1/2} D_{L,28.3}^{-2} \text{ Jy}. \quad (13)$$

The maximum Lorentz factor attainable by the electrons is calculated by equating the acceleration timescale in the shock to the radiation timescale, which gives $\gamma_M = (3q_e/g_M \sigma_T B'_{FS})^{1/2} \sim 5.4 \times 10^6 \eta_{600}^{-1/2} \epsilon_{B,-1}^{-1/4} n_0^{-1/4}$, where g_M is a numerical factor of order unity. The corresponding photon energy is $\varepsilon_{FS,M} = 3hq_e B'_{FS}/(4\pi m_e c) \gamma_M^2 \eta/(1+z) = 11.2 \eta_{600} ((1+z)/2)^{-1} \text{ GeV}$.

The scattering optical depth in the FS is given by

$$\tau_{FS} = \frac{N_e \sigma_T}{4\pi R^2} = \frac{4\pi r_{dec}^3 n \sigma_T}{3 \times 4\pi r_{dec}^2} = 1.1 \times 10^{-8} L_{t,53}^{1/3} (1 - \zeta_r)^{1/3} t_{1.3}^{1/3} \eta_{600}^{-2/3} n_0^{2/3} \quad (14)$$

where N_e is the number of electrons in the forward shock.

4.2. Reverse Shock (RS) Synchrotron

The reverse shock, if it develops, becomes strongest at the deceleration radius. A contact discontinuity (CD) separates the FS from the RS, and in the frame of the CD the RS travels backwards. The pressure is the same in both sides of the CD, and consequently the magnetic energy density will be the same as well, under the usual assumption that the magnetic field is turbulently generated and ϵ_B is taken to be the same in both sides.

The characteristic frequencies for the RS will be: $\varepsilon_m^{RS} = \varepsilon_m^{FS}/\Gamma^2 = 1.1 \times 10^{-5} \epsilon_{B,-1}^{1/2} \epsilon_{e,-2}^2 n_0^{1/2} \eta_{600}^2 g_{p,2.4}^2 \left(\frac{1+z}{2}\right)^{-1} \text{ keV}$ and $\varepsilon_c^{RS} = \varepsilon_c^{FS}$ (e.g. Sari & Mészáros 2000). The RS cooling frequency can differ by about 10%, but we will ignore this

difference. Generally the RS peak flux will be a factor Γ higher than in the FS. In our case the radiative regime changes from the FS to RS: while the FS electrons are in fast cooling, the reverse shock is in the slow cooling case. We calculate the peak flux $F_{\nu,max}^{RS}$ from

$$F_{max}^{RS}(\varepsilon_m) = \frac{N_e P_{max}(\nu)}{4\pi D_L^2} = \frac{L_k t_0}{\eta m_p c^2} \frac{m_e c^2 \sigma_T \eta B}{3q_e} \frac{1}{4\pi D_L^2} = 92 L_{t,53} (1 - \zeta_r) t_{1.3} \eta_{600} \epsilon_{B,-1}^{1/2} n_0^{1/2} D_{L,28.3}^{-2} \text{ Jy}. \quad (15)$$

It is unclear, in an initially magnetically dominated outflow, whether the RS will develop or not, depending on various assumptions (Zhang & Kobayashi 2005; Giannios et al. 2008; Zhang & Yan 2011; Narayan et al. 2011). In the simplest cases the Alfvénic $\gamma'_A \sim \sqrt{1 + \sigma}$ Lorentz factor will be high and magnetic waves can carry information from the CD to the start of the ejecta, suppressing the RS. Here $\sigma \approx F_{\varepsilon,r}/F_{\varepsilon,k}$ is the magnetization parameter giving the ratio of the Poynting (magnetic) flux to the kinetic flux. However, the result depends on the amount of dissipated magnetic energy at radii before reaching the deceleration radius. If there is significant portion of magnetic energy compared to the kinetic energy there may be no reverse shock, while in the contrary case reverse shocks may form.

The optical depth of the RS region is important for calculating the flux of the inverse Compton radiation. We calculate the optical depth of the RS at r_{dec} from

$$\tau_{RS} = \frac{N_e \sigma_T}{4\pi R^2} = \frac{L_k t_0 \sigma_T}{\eta m_p c^2 4\pi r_{dec}^2} = 6.4 \times 10^{-6} L_{t,53}^{1/3} (1 - \zeta_r)^{1/3} t_{1.3}^{1/3} \eta_{600}^{1/3} n_0^{2/3} \quad (16)$$

where N_e is the number of electrons in the reverse shock. Note that at r_{dec} the optical depth of the RS is η times the optical depth of the FS as expected.

4.3. Forward Shock Self-Compton (FS-SSC)

At the deceleration radius the forward shock (and the reverse shock, if present) accelerated electrons will cool also by inverse Compton interactions with their own synchrotron photons. The forward shock at the deceleration is in the synchrotron fast cooling regime, for the parameters considered here, and the Compton parameter is $Y = (-1 + \sqrt{1 + 4\eta_{SSC}\epsilon_e/\epsilon_B})/2 \approx \epsilon_e/\epsilon_B = 0.1$, where $\eta_{SSC} = \min((\gamma_e/\gamma_m)^{2-p}, 1)$ and $\eta_{SSC} = 1$ is valid for the fast cooling case.

The SSC component of the FS will also be in the fast cooling radiative regime, and the minimal and the cooling energies will be given by $\varepsilon_m^{SSC} \approx 2\gamma_m^2 \varepsilon_m =$

$75 \epsilon_{B,-1}^{1/2} \epsilon_{e,-2}^4 n_0^{1/2} \eta_{600}^6 g_{2.4}^4 ((1+z)/2)^{-1}$ GeV and $\epsilon_c^{SSC} \approx 2\gamma_c^2 \epsilon_c = 70 L_{t,53}^{-4/3} (1 - \zeta_r)^{-4/3} t_{1.3}^{-4/3} \epsilon_{B,-1}^{-7/2} n_0^{-13/6} \eta_{600}^{2/3} (1+Y)^{-4} ((1+z)/2)^{-1}$ keV respectively.

The amplitude of the FS SSC component is determined from: $(\epsilon^{SSC} F_\epsilon)_{\text{peak}}^{SSC} = Y \epsilon_m^{FS} F_{\epsilon_m}^{FS} = 3.7 \times 10^{-9} L_{t,53}^{2/3} (1 - \zeta_r)^{2/3} t_{1.3}^{2/3} \eta_{600}^{8/3} n_{1/3} \epsilon_{e,-2}^1 g_{p,2.4}^1 D_{L,28.3}^{-2}$ erg cm⁻² s⁻¹. The higher energy electrons can reach the Klein-Nishina (KN) regime. This results in a break in the spectrum at $\epsilon_{KN,c}^{SSC} = \gamma_c m_e c^2 \eta / (1+z) = 15 L_{t,53}^{-1/3} (1 - \zeta_r)^{-1/3} t_{1.3}^{-1/3} \epsilon_{B,-1}^{-1} n_0^{-1/3} \eta_{600}^{1/3} (1+Y_{SSC})^{-1}$ GeV. Details of the KN break energy are in Appendix B.

4.4. EIC scattering of photospheric nonthermal photons on external forward shock electrons (FS-EIC)

The electrons in the forward shock will also lose energy by external inverse Compton (EIC) as they upscatter the photons from the prompt emission (photospheric) region. This effect was discussed by Beloborodov (2005) for interaction of the prompt photons with both FS and RS. It was further proposed that a delay of the order observed by Fermi arises within this setup (see also Meszaros & Rees (1994)). The minimum and cooling frequencies of this component will be $\epsilon_m^{EIC} \approx 2\gamma_m^2 \epsilon_{br} = 6.2 \zeta_r^{-1/2} (1 - \zeta_r)^{1/2} \epsilon_{B,0}^{1/2} \epsilon_{e,-2}^2 \eta_{600}^2 g_{p,2.4}^2 r_{0,7}^{-1/2} \Gamma_r^3 ((1+z)/2)^{-1}$ TeV and $\epsilon_c^{EIC} \approx 2\gamma_c^2 \epsilon_{br} = 6.0 L_{t,53}^{-2/3} \zeta_r^{-1/2} (1 - \zeta_r)^{-1/6} t_{1.3}^{-2/3} \epsilon_{B,-1}^{1/2} \epsilon_{B,0}^{-2} n_0^{-4/3} \eta_{600}^{-2/3} (1+Y)^{-2} r_{0,7}^{-1/2} \Gamma_r^3 ((1+z)/2)^{-1}$ GeV, where we differentiate between prompt and FS magnetic parameter by using $\epsilon_{B,0}$ and $\epsilon_{B,-1}$ respectively.

In the absence of KN suppression, the flux of the FS EIC emission would be of the form (Murase et al. 2011):

$$F_\epsilon^{FSEIC} \propto \begin{cases} \epsilon^{1-\alpha} & \text{if } \epsilon \leq \epsilon_{EIC,c} \\ \epsilon^{-1/2} & \text{if } \epsilon_{EIC,c} < \epsilon \leq \epsilon_{EIC,m} \\ \epsilon^{-p/2} & \text{if } \epsilon_{EIC,m} < \epsilon \end{cases} \quad (17)$$

The KN effects however would introduce breaks in the high-energy part of the spectrum. Details of the derivation of the KN frequencies are in Appendix B. For a large part of the parameter space, $\epsilon_{EIC,m}$ will be in the KN regime, and the ϵF_ϵ peak will be at the KN break frequency $\epsilon_{KN}^{EIC} \approx \eta \gamma_c m_e c^2 / (1+z) = 15 (1 - \zeta_r)^{-1/3} L_{t,53}^{-1/3} t_{1.3}^{-1/3} \epsilon_{B,-1}^{-1} n_0^{-2/3} \eta_{600}^{2/3} (1+Y)^{-1} ((1+z)/2)^{-1}$ GeV. A rough estimate of the peak of the EIC emission at the peak is

$$(\epsilon F_\epsilon)_{EIC}^{\text{peak}} \sim \epsilon_{br} N_{\epsilon,p} \tau_{FS} \epsilon_{KN}^{EIC} = \quad (18)$$

$$7.2 \times 10^{-10} L_{t,53} \zeta_r^{3/2} (1 - \zeta_r)^{-1/2} \epsilon_{B,0}^{-1/2} \epsilon_{B,-1}^{-1} \Gamma_r^{-3} (1 + Y)^{-1} D_{L,28.2}^{-2} \text{ erg cm}^{-2} \text{ s}^{-1} \quad (19)$$

where $N_{\epsilon,p}$ is the photon number spectrum of the prompt emission, evaluated here for $\alpha = 1$, $\beta = 2.4$ and for $\epsilon \approx \epsilon_{br}$. To account for the anisotropy of the emitted radiation in the forward shock frame, we multiply our flux by a factor of 0.5 (Fan & Piran 2006).

4.5. EIC scattering of photospheric non-thermal photons on external reverse shock electrons (RS-EIC)

If the reverse shock develops, there will be an external inverse Compton component from the reverse shock electrons scattering prompt photons as well. This differs from the forward shock EIC because of the larger optical depth and the lower energy of the electrons in the RS, and because the RS will be in the slow cooling phase. The characteristic frequencies are $\epsilon_m^{RSEIC} \approx 2\gamma_{RS,m}^2 \epsilon_{br} = 17 \epsilon_{e,-2g_{p,2.4}} r_{0,7} \epsilon_{B,0}^{1/2} \Gamma_r^3 ((1+z)/2)^{-1}$ MeV and $\epsilon_c^{RSEIC} \approx 2\gamma_{RS,c}^2 \epsilon_{br} = 6.0 L_{t,53}^{-2/3} \zeta_r^{-1/2} (1 - \zeta_r)^{-1/6} t_{1.3}^{-2/3} \epsilon_{B,0}^{1/2} \epsilon_{B,-1}^{-2} n_0^{-4/3} \eta_{600}^{-2/3} (1 + Y)^{-2} r_{0,7}^{-1/2} \Gamma_r^3 ((1+z)/2)^{-1}$ GeV. The RS electrons, being in the slow cooling phase, will upscatter the prompt emission into a spectrum of the following shape:

$$F_\epsilon^{RSEIC} \propto \begin{cases} \epsilon^{1-\alpha} & \text{if } \epsilon \leq \epsilon_m^{RSEIC} \\ \epsilon^{(1-p)/2} & \text{if } \epsilon_m^{RSEIC} < \epsilon \leq \epsilon_c^{RSEIC} \\ \epsilon^{-p/2} & \text{if } \epsilon_c^{RSEIC} < \epsilon. \end{cases} \quad (20)$$

The peak of the emission will be at the Klein Nishina cutoff frequency for this component, which is $\epsilon_{KN}^{RSEIC} \simeq \eta \gamma_m^{RS} m_e c^2 / (1+z) \approx 0.8 \eta_{600} \epsilon_{e,-2g_{p,2.4}} ((1+z)/2)^{-1}$ GeV. This introduces a spectral break and the photon index above this energy will be $\sim -(\alpha - p - 2)$.

The peak flux of the emission, considering a weakening by 0.5 due to anisotropy, is

$$\epsilon F_{\epsilon,RSEIC}^{\text{peak}} \approx \epsilon_{br} N_{\epsilon,p} \tau_{RS} \epsilon_{KN}^{RSEIC} = 2.3 \times 10^{-8} L_{t,53}^{4/3} \zeta_r^{3/2} (1 - \zeta_r)^{-1/6} t_{1.3}^{1/3} \eta_{600}^{4/3} n_0^{2/3} \Gamma_r^3 r_0^{-1/3} \epsilon_{B,0}^{-1/2} \epsilon_{e,-2g_{p,2.4}} D_{L,28.2}^{-2} \quad (21)$$

Note that $\epsilon_{KN}^{RSEIC,m}$ falls in the low-energy part of the *Fermi LAT* range. Thus, if the RS-EIC were dominant, the photon index expected would be $-(\alpha - p - 2) \approx 3.4$. In bursts with extra high-energy components, such soft photon indices (or even softer) are indeed observed. For other model parameters, we found that while

the RS-EIC is the dominating component at its peak, other inverse Compton radiation components such as FS-EIC or FS-SSC can make the spectrum harder by contributing at a few $\times 10$ GeV s.

5. Numerical Results and Model Parameter Variations

We calculated a number of model spectra based on the considerations of the previous sections. The initial set of nominal parameters used is $L_t = 10^{53}$ erg/s, $t = 20$ s, $\zeta_r = 0.5$, $\zeta_k = 0.5$, $n = 1$ cm $^{-3}$, $\eta = 600$, $\epsilon_{B,pr} = 1$, $\epsilon_{B,FS} = \epsilon_{B,RS} = 0.1$, $\epsilon_{e,FS} = \epsilon_{e,RS} = 0.01$, $r_0 = 10^7$ cm, $z = 1$, $D_L \approx 2 \times 10^{28}$ cm.

Here $\zeta_r = 0.5$ is the nominal fraction of the initial L_t assumed to be radiated at the photosphere in non-thermal and thermal radiation, $\zeta_k = 0.5$ is the energy radiated by the external shock at the deceleration radius. Also, for simplicity, when a reverse shock forms, we assume the same values for ϵ_B and ϵ_e in both the forward and in the reverse shocks. We have explored also the effects of departures from these various nominal parameters.

Models with Negligible Pair Formation.- A first set of models was calculated assuming that the first scenario of §3.1, where the photospheric spectrum of eq. (7) cuts off around $m_e c^2$ in the jet frame, or around ~ 50 MeV in the observer frame, with pair formation being negligible in both the photosphere and in the external shock. The resulting generic observer-frame spectrum consists of a Band function spectral component peaking at sub-MeV energies and extending up to ~ 50 MeV, with a second component at GeV energies due to a combination of EIC and SSC by external forward and reverse shock electrons of photospheric photons and their own synchrotron photons. This second GeV component has typically a total fluence which is $\lesssim 0.1$ that of the MeV Band function, and for some parameter ranges it stands out from the first component, while for others it merges more or less smoothly with the high energy branch of the first component. Whether it stands out or not depends on the external density, the external shock parameters, and on whether a reverse shock forms or not.

In Figure 1 we show one of the cases where the second, GeV component, stands out from the first Band component. The parameters of the external forward shock are $\epsilon_B = 0.01$ and $\epsilon_e = 0.02$, and the dissipative photosphere produces a Band function peaking at $\lesssim 1$ MeV in the *GBM* range.

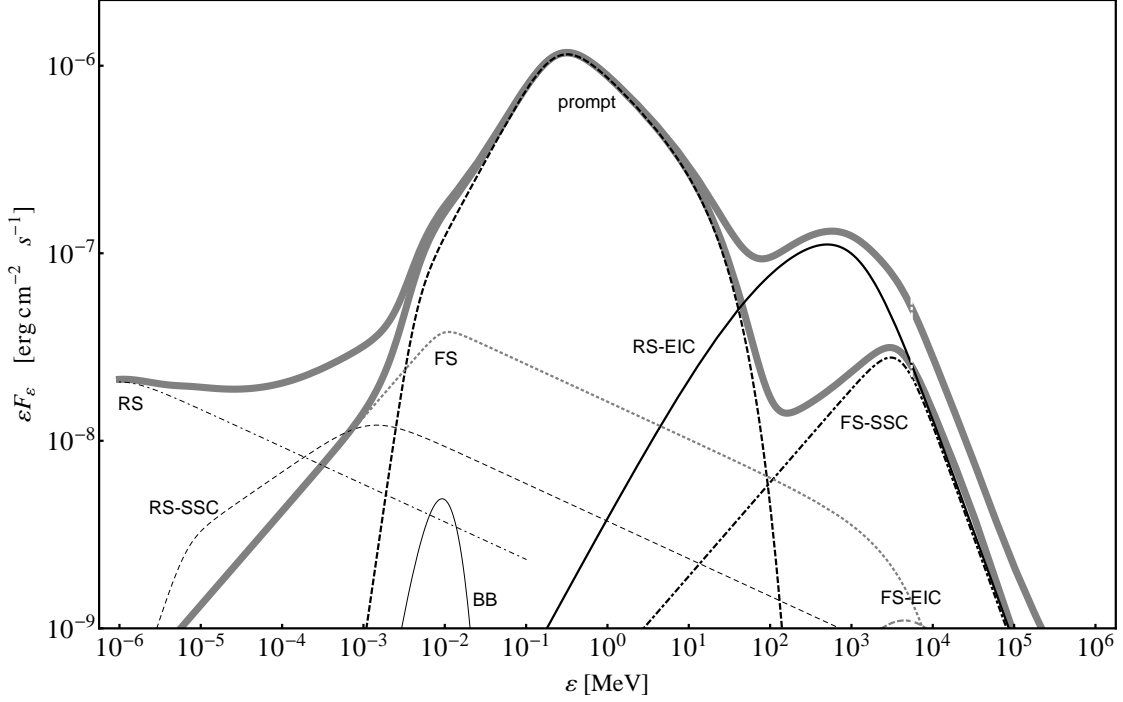


Fig. 1.— A model without pair formation, $L_t = 5 \times 10^{52}$ erg/s, $t = 20$ s, $\zeta_r = 0.6$, $\zeta_k = 0.4$, $n = 100$ cm $^{-3}$, $\eta = 400$, $\epsilon_{B,pr} = 0.9$, $\epsilon_{B,FS} = 1 \times 10^{-2}$, $\epsilon_{e,FS} = 2 \times 10^{-2}$, $r_0 = 10^7$ cm, $z = 1$, $\beta = 2.4$, $p = 2.4$. The black dashed line is the prompt synchrotron emission, black thin continuous line is the prompt thermal component (marked BB), the thick black line is the RS-EIC, the gray, thick, dotted line is the forward shock synchrotron part (FS), the gray, dashed line is the forward shock external inverse Compton, the black dash-dotted is the FS-SSC component, the gray, dashed line is the RS-SSC and the gray, dash-dotted is the RS synchrotron component. The thick gray continuous line is the sum of the components (the upper one is with and the lower one without the RS contributions).

In the *LAT* range, if a reverse shock is present, we can see a clear “bump” in the spectrum around 1 GeV (the upper thick curve). The prompt emission and the bump up to ~ 3 GeV in Figure 1 is strikingly similar to the spectrum of GRB 090926A (Ackermann & the Fermi collaboration 2011, their figure 5.), which showed an extra power law with a cutoff besides the Band component. Here the extra power law would be the rising part of the RS-EIC (the model photon index $-(-p - 1)/2 \simeq 1.7$ coincides precisely with the measured one for $p = 2.4$) and the cutoff is the part after the RSEIC peak. The ratio between the *GBM* and *LAT* fluences is $\sim 10^{-1}$, an average ratio in the observed bursts (Omodei & the Fermi LAT collaboration 2011; Pelassa 2011). At optical wavelengths the reverse shock produces a high flux ($\sim 3 \times 10^{-8}$ erg cm $^{-2}$ s $^{-1}$, or $m_R \sim 7$) which could be responsible for the very bright optical flashes observed in some bursts.

However, if the reverse shock is weak or missing, in the same figure 1 the upper thick bump at ~ 1 GeV is absent, and is replaced by the lower thick line. One has the same *GBM* prompt emission and a hard component emerging at $\lesssim 10$ GeV. This component would also appear as an extra power-law component, but in this case, it is weaker by one order of magnitude than the prompt emission. For the low photon number detected in this energy range, such a component might have low significance in a fit. Also the optical flux is much lower, 3×10^{-10} erg cm $^{-2}$ s $^{-1}$, or $m_R \sim 11.8$. We note that the combination of parameters used for obtaining the single component and two component spectra in this figure are not unique.

In Figure 2 we show one of the cases where the overall spectrum appears as a single Band component, due to the second GeV component approximating an extension of the first, MeV Band component. The parameters of the external shock are in this case $\epsilon_B = 0.02$, $\epsilon_e = 0.005$ for both the forward and reverse shock, with $\eta = 400$ and $n = 30$ cm $^{-3}$, other parameters being nominal. It is seen that the combination of the external reverse shock EIC and the forward shock SSC plus EIC provides a roughly continuous slope connecting the MeV Band spectrum to the high energy branch (the upper thick curve from ~ 0.1 GeV onwards). The reverse shock EIC hump fills in the through left by the forward shock SSC. The wiggles from the two humps at 100 MeV and 10 GeV would be smoothed out in typical spectral fits with low photon number statistics in this range encountered in *Fermi LAT* bursts. The matching of the flux levels between the photospheric spectrum high energy end and the external RS peak is controlled largely by the external density n , whose value here is in the usual range.

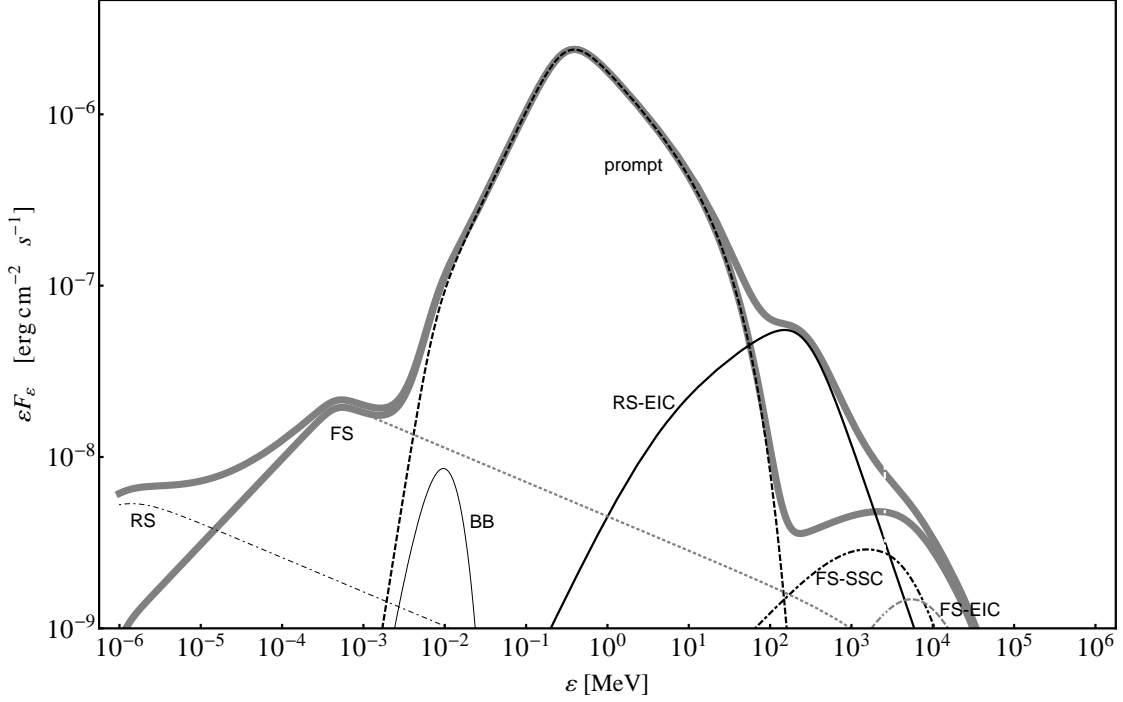


Fig. 2.— A different model, also without pair formation, and parameters $L_t = 10^{53}$ erg/s, $t = 20$ s, $\zeta_r = 0.5$, $\zeta_k = 0.5$, $n = 30$ cm $^{-3}$, $\eta = 400$, $\epsilon_{B,pr} = 1$, $\epsilon_{B,FS} = \epsilon_{B,RS} = 2 \times 10^{-2}$, $\epsilon_{e,FS} = \epsilon_{e,RS} = 5 \times 10^{-3}$, $r_0 = 10^7$ cm, $z = 1$, $\beta = 2.5$, $p = 2.4$. The black dashed line is the prompt synchrotron emission, black thin continuous line is the prompt thermal component (marked BB), the thick black line is the RS-EIC, the gray, thick, dotted line is the forward shock synchrotron part (FS), the gray, dashed line is the forward shock external inverse Compton, the black dash-dotted is the FS-SSC component and the gray, dash-dotted is the RS synchrotron component. The thick gray continuous line is the sum of the components (the upper one is with and the lower one without the RS contributions).

Assuming that a reverse shock is absent or negligibly weak (i.e. ignoring the upper thick gray continuous line in fig. 2 peaking at $\gtrsim 100$ MeV), one sees that now a second hard component appears above 100 MeV and peaks at 3 GeV, being in this case mainly due to the forward shock SSC, with a contribution from the EIC of photospheric photons. Other components, while present, are here subdominant. The secondary peak (also in the absence of the RS-EIC component in fig. 2), though reminiscent of the extra power-law component observed in GRB 090902B or 090926A, is ~ 2 orders of magnitude fainter than the main peak, while in the observed cases this ratio, when reported, is at most ~ 1.5 . The optical flux predictions are $m_R \sim 8.3$ and $m_R \sim 10.5$ in the presence or absence of the reverse shock. Again, this is not the sole combination of parameters which produces an approximate single Band function extending to GeV energies.

In the above models where pair formation is not expected, the qualitative effects of increasing the terminal Lorentz factor η consists in a strengthening of the RS-EIC component. Even though at low η we expect a lower cutoff for the prompt emission and a more prominent inverse Compton component, this is not the case. Below $\eta \simeq 300$ the main high-energy component is the sum of the FS-SSC, the FS-EIC and the prompt SSC at ~ 10 GeV which form a distinct peak. Increasing the density n makes the RS-EIC component to be more detectable from $n \simeq 10 \text{ cm}^3$ up to $n \simeq 500 \text{ cm}^3$. Outside these parameters the FS-SSC and the FS-EIC are the same magnitude or dominating the RS-EIC component and a break in the spectrum is more visible. The shape of the high energy part of the spectrum has only a weak dependence on the value of ϵ_B . By decreasing the prompt magnetic parameter, the peak energy becomes lower and the external components could become more prominent.

Models with Pair Formation.— A second set of models was calculated assuming that the Band spectrum from the photosphere extends to sufficiently high energies that pair formation from $\gamma\gamma$ interactions is expected (see §3). In these cases the primary Band component extends up to an energy given by eq.(9), and there is a secondary synchrotron component from the $\gamma\gamma$ pairs, both the primary and secondary photons leading to separate SSC and EIC components from upscattering in the photosphere and in the forward and reverse external shock, some components being more important than others. Figure 3 presents one of the cases involving pair production. The overall behavior is not too different from that of the models with no pair production: the RS-EIC component is approximately smoothly joined to the prompt at ~ 100 MeV. The RS-EIC in turn joins smoothly to the other

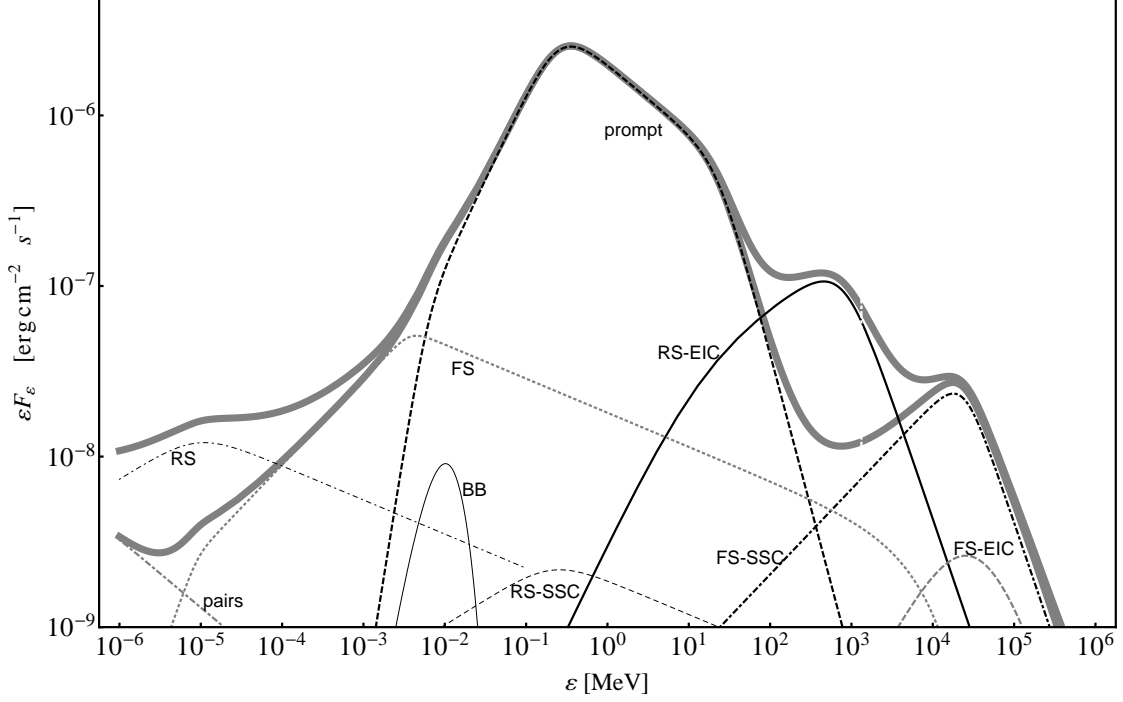


Fig. 3.— Model with pair formation with $L_t = 10^{53}$ erg/s, $t = 20$ s, $\zeta_r = 0.6$, $\zeta_k = 0.4$, $n = 10$ cm $^{-3}$, $\eta = 600$, $\epsilon_{B,pr} = 1$, $\epsilon_{B,FS} = \epsilon_{B,RS} = 1 \times 10^{-2}$, $\epsilon_{e,FS} = \epsilon_{e,RS} = 1 \times 10^{-2}$, $r_0 = 10^7$ cm, $z = 1$, $\beta = 2.4$, $p = 2.4$. The black dashed line is the prompt synchrotron emission, black thin continuous line is the prompt thermal component (marked BB), the thick black line is the RS-EIC, the gray, thick, dotted line is the forward shock synchrotron part (FS), the gray, dashed line is the forward shock external inverse Compton, the black dash-dotted is the FS-SSC component, the gray, dash-dotted is the RS synchrotron component and the thick dash-dotted is the pair synchrotron contribution. The thick gray continuous line is the sum of the components (the upper one is with and the lower one without the RS contributions).

higher energy components at ~ 10 GeV. If a RS does not develop, the only missing component at high energies will be the RS-EIC (thick black line) and again we get a bump in the spectra at ~ 10 GeV energies. The optical flux is only about 1.3 magnitudes fainter in the absence than in the presence of the reverse shock, $m_R \sim 9.3$ and ~ 8 for the two cases.

In Figure 4 we show another case where pair formation occurs, for a different choice of parameters. In this case the second component bump would be present irrespective of whether the reverse shock is present or absent, since both shocks result in a similar bump. The FS synchrotron and the FS-EIC contribute significant flux to the bump. In this case, the optical flux with the reverse shock is larger, $m_R \sim 5.5$, and much fainter in the absence of the reverse shock, $m_R \sim 10$.

Low Energy Power Law Extensions.- A notable feature of Figs. 1 through 4 is that the forward shock synchrotron radiation extends into the optical range. In Asano et al. (2010), such a power law extending into the optical was obtained for a hadronic cascade GRB model. Here it arises in a purely leptonic mode. For reasonable parameters this component falls between the cooling and the characteristic synchrotron frequencies. One sees that, for bright *Fermi LAT* bursts, in the absence of pair formation the forward shock synchrotron can produce a prompt optical flash of $m_R \gtrsim 11 - 12$, even in the absence of a reverse shock. This visual flux scales with the prompt photon luminosity L_r . A conversion of the flux units to R-magnitudes is $10^{-8} \text{ erg cm}^{-2} \text{ s}^{-1} \rightarrow m_R \sim 8.0$, and $10^{-10} \text{ erg cm}^{-2} \text{ s}^{-1} \rightarrow m_R \sim 13.0$, with the usual five magnitudes interval per each factor 100 increase in flux. In the cases where pair formation occurs, the pairs contribute an additional synchrotron component, which in the optical range predicts an even brighter prompt flash. This is seen in Fig. 3, with the source at $z = 1$. In both types of models (with or without pair formation), in the cases where a reverse shock is present the optical flashes can be significantly brighter, in the range $m_R \sim 6 - 8$ at the same redshift.

6. Discussion

We have addressed the high-energy spectral properties of the bursts observed with *Fermi LAT*, using a magnetically dominated outflow model where the prompt MeV emission arises in the photosphere, and high energy components arise from inverse Compton scattering by both photospheric and external shock electrons.

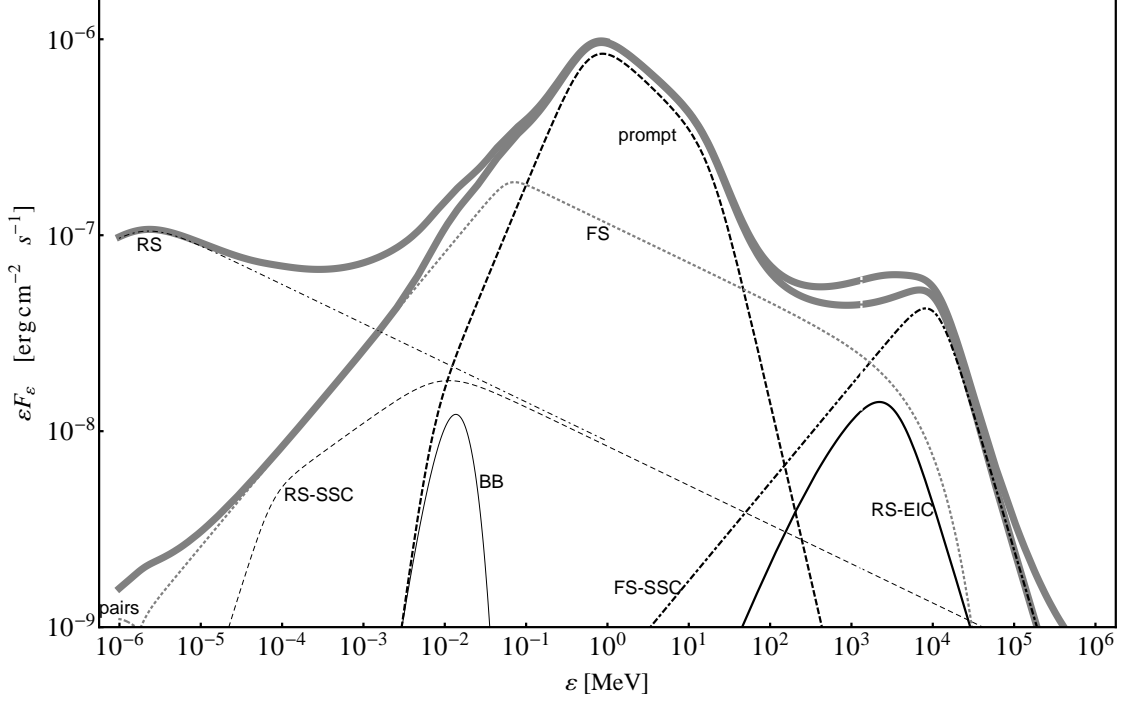


Fig. 4.— Another model with pair formation, and parameters $L_t = 10^{53}$ erg/s, $t = 20$ s, $\zeta_r = 0.2$, $\zeta_k = 0.8$, $n = 1$ cm $^{-3}$, $\eta = 600$, $\epsilon_{B,pr} = 1$, $\epsilon_{B,FS} = \epsilon_{B,RS} = 0.1$, $\epsilon_{e,FS} = \epsilon_{e,RS} = 1 \times 10^{-2}$, $r_0 = 10^7$ cm, $z = 1$, $\beta = 2.4$, $p = 2.4$. The black dashed line is the prompt synchrotron emission, black thin continuous line is the prompt thermal component (marked BB), the thick black line is the RS-EIC, the gray, thick, dotted line is the forward shock synchrotron part (FS), the gray, dashed line is the forward shock external inverse Compton, the black dash-dotted is the FS-SSC component, the gray, dash-dotted is the RS synchrotron component and the thick dash-dotted is the pair synchrotron contribution. The thick gray continuous line is the sum of the components (the upper one is with and the lower one without the RS contributions).

We have investigated circumstances under which a single Band function appears to extend to the highest energies detected by the *Fermi LAT*, and where a second high energy component shows itself above the MeV range Band spectrum. We have also addressed, in the same context, the production of prompt optical flashes.

We find that, qualitatively, these types of models are able to explain the observed diversity of *GBM* and *LAT* prompt emission spectra, without invoking an internal shock emission at intermediate radii. The presence or relative strength of a reverse shock plays a role in determining the spectral shape and the basic dichotomy in the latter. As discussed by, e.g. Narayan et al. (2011); Mimica & Aloy (2011); Giannios et al. (2008), for modest magnetization σ of the outflow a reverse shock may be expected; and while for initially magnetically dominated outflows σ (or ϵ_B) is still large at the photosphere, at larger radii it can be expected to drop sufficiently low to make reverse shocks possible, although uncertainties remain concerning the threshold magnetization and the reverse shock strength. Thus, we assumed that within the normal range of parameters, reverse shocks may be important in some bursts and not in others. When a reverse shock is absent, the forward shock results in a distinct high energy (GeV) spectral component, whose fluence is 1-2 orders of magnitude below that of the Band component. In these cases, the effective high energy slope β of the Band component appears rather soft, in agreement with data discussed in, e.g. Zhang et al. (2011). On the other hand, when a reverse shock is present, its inverse Compton radiation can result in a larger fluence extra high energy component, 0.5-1 orders of magnitude below the Band fluence; or it can result in a smooth continuation of the Band component, which can mimic a single Band high energy component of relatively hard effective slope β . The relatively small number of photons observed in this band could result in fits where the slight wiggles in the theoretical spectra are largely ironed out.

The fact that the *LAT* emission is contributed by the external shock implies that it will appear with an intrinsic delay of order $t_{del} \sim r_{dec}(1+z)/c\eta^2 \approx 4.4 L_{t,53}^{1/3} (1 - \zeta_r)^{1/3} t_{1.3}^{1/3} n_0^{-1/3} \eta_{600}^{-8/3} (1+z)/2$ s, of order a few seconds relative to the photospheric MeV component. Such a delay was indicated also in some early work on *LAT* spectra (e.g., Ghisellini et al. 2009; Kumar & Barniol Duran 2009), where, however, the *LAT* emission was attributed to the forward shock synchrotron radiation. In our case, it is the inverse Compton components of the forward or reverse shock which dominate the *LAT* emission.

The implications of our model for constraints on the bulk Lorentz factor are

much less stringent than in one-zone models where the *GBM* and *LAT* emission are assumed to arise in the same region. E.g., in Abdo & the Fermi collaboration (2009); Ackermann & the Fermi collaboration (2011); Abdo et al. (2009), such analyses indicated Lorentz factors $\gamma \sim 800 - 1000$ or higher. However (Zou et al. 2011; Pe’er 2011; Zhao et al. 2011) in generic two-zone models the Lorentz factor need not be so large. Specifically, in our model, which is a two-zone model in which the high energy photons arise in the external shock, the compactness parameter in the latter is low, and the spectra can be reproduced with terminal Lorentz factors $\Gamma \sim \eta \sim 300 - 600$.

As discussed in §3.1, the magnetized dissipative photosphere can produce a Band-like non-thermal spectrum resembling the observations. In our magnetized models, in the absence of pair formation this component cuts off above ~ 50 MeV, or in the presence of pair formation, it steepens by one power law index above ~ 100 MeV. Recently Kocevski & The Fermi Collaboration (2012) analysed the paucity of GRBs measured by LAT. They claim that nearly half of the bursts detected by GBM which were in the LAT field of view required a break under 0.1 GeV to explain the nondetection by LAT. In the framework of this model these results mean that there is indeed a cutoff at $\sim 50 - 100$ MeV. This is either due to a softening because of pair creation or a cutoff according to the magnetic acceleration mechanism.

Recently Yonetoku et al. (2011) reported a polarization measurement in the prompt emission from GRB 100826A. This could be an indication of a magnetically dominated photosphere (Waxman 2003; Nakar et al. 2003), although polarization might also be expected from processes not requiring strong magnetic fields (e.g., Lazzati et al. 2004). For a magnetic jet, the transverse field components will dominate in the emission region, and while for an observer line of sight along the jet axis the polarization could average itself out, for the larger probability off-axis viewing directions a net polarization could be expected.

The magnetic photosphere models also predict a weaker thermal component peaking at a few keV (§3.2), plotted in Figs. 1 through 4. Such a thermal component has been reported in Guiriec et al. (2011) for GRB 100724B. In our models such a component appears at approximately the right energies, its fluence generally being low compared to the nonthermal components. However, only for a relatively small range of parameters would it appear possible to detect it. One problem is that it can be conflated with the contribution of the forward shock

synchrotron, e.g. as the bump around $\lesssim 10$ keV in Fig. 3.

Another interesting component is the optical band extension of the external shock synchrotron spectra (see Figs. 1 through 4). It is seen that just the external forward shock by itself already can produce optical flashes of $m_R \gtrsim 12$ (Figs. 1, 2), while if pair formation occurs in the photosphere, the cooled pairs there can lead to flashes of $m_R \sim 9.3$ (Figs. 3, 4) or even brighter for suitable sets of parameters. On the other hand, when a reverse shock is present, its synchrotron component naturally produces a bright prompt optical flash, as known for quite a while (e.g., Meszaros & Rees 1993, 1997). Here, in addition, we have considered also the IC components of the reverse shock, and the effect of a photospheric EIC component as well. For reasonable parameters, the flux can be close to few $\times 10^{-7}$ erg cm $^{-2}$ s $^{-1}$ in the optical band, which translates to m_R brighter than 7 at $z = 1$. Generically, the relative scarcity of observed optical flashes may be attributed to the fact that their brightness scales roughly the same way as the prompt GeV luminosity ($(\varepsilon F_\varepsilon)_{\text{peak}}^{RS} \propto L_t^{p/3} \propto L_t^{0.8}$, $(\varepsilon F_\varepsilon)_{\text{peak}}^{\text{prompt}} \propto L_t$ and $(\varepsilon F_\varepsilon)_{\text{peak}}^{RS-EIC} \propto L_t^{4/3}$), as well as to the fact that reverse shocks may be rare in magnetically dominated outflows.

For the naked eye GRB 080319, the roughly similar behavior of the optical and γ -ray light curves can be used to argue for a common origin of both (Racusin et al. 2008). However, the optical light curve is not sampled as well as the γ -ray light curves, and at least in the prompt phase shows temporal structures (peaks) comparable in duration to the deceleration time which could be compatible with a reverse shock origin, although the RS origin was disfavoured by Racusin et al. (2008). On the other hand, a fast variability of the prompt optical flash might be suggestive of an origin in the same region as the prompt MeV emission, which might be attributed to the photospheric cooled pair synchrotron component. However, only very rare parameter combinations could push the optical flux of the pair synchrotron component up to $m_R \sim 5$ as in the naked eye burst (Racusin et al. 2008). E.g. in our model a combination of $\eta \sim 1000$, $\beta \approx 2.1$ and $\zeta_r \approx 0.99$ would approach such brightnesses.

Concerning the FS-EIC and RS-EIC components, strictly speaking for these it is not necessary to invoke the magnetically dominated jet model. Indeed, similar results can be obtained by a baryonic model as well Beloborodov (2005, 2010). In magnetic and baryonic cases the delay between the MeV and GeV components will be a few seconds, comparable to the values measured by *Fermi*.

We note that this model may be applicable both to long and short bursts,

since a magnetized photosphere and an external shock would be expected in both cases. The relatively shorter GeV-MeV delays in the short burst cases could be understood in terms of a closer-in deceleration or a larger Lorentz factor, the latter being suggested also by their harder MeV spectra.

Finally, we point out that the predicted inverse Compton components in these models extend into the TeV range, for a range of parameters. The photon with the highest energy detected by *LAT* from a GRB had an energy of ~ 33 GeV (Abdo & the Fermi collaboration 2009). However, the spectral features above this energy are in the range of ground-based Cherenkov telescopes, including also HAWC and the future CTA, providing potentially interesting targets for such detectors.

We acknowledge NASA NNX09AL40G, NSF PHY-0757155 and OTKA grant K077795 for partial support, and thank Bin-Bin Zhang, Shan Gao, Kenji Toma and the referee for useful comments.

A. Other Radiation Components

Other electron inverse Compton components, besides those already discussed, may be present if a reverse shock develops. In this case one would expect scattering of reverse shock photons on the forward shock electrons, and FS photons on the RS electrons. Both of these components have a flux density (He et al. 2011) $\tau_{FS} F_{\epsilon_{\max}}^{RS} \approx \tau_{RS} F_{\epsilon_{\max}}^{FS} \approx 10^{-6}$ Jy peaking at $\epsilon \approx 0.1$ keV with a flux of $(\epsilon F_{\epsilon})_{\text{peak}} \approx 2 \times 10^{-13}$ erg cm $^{-2}$ s $^{-1}$, which makes them negligible compared to other (e.g. FS or RS) components.

The external inverse Compton radiation of the pair synchrotron photons on the FS and the RS will also give a flux of the order 5×10^{-10} erg cm $^{-2}$ s $^{-1}$ at 80 MeV and 0.4 MeV respectively.

The prompt thermal (blackbody) component will also be upscattered at the FS as well at the RS (Ando & Mészáros 2008). Both components consist of a set of smoothly joined power-laws and a cutoff at high energies. The BB-FS-EIC has a peak of 9×10^{-12} erg cm $^{-2}$ s $^{-1}$ at ~ 30 GeV while the BB-RS-EIC has a peak of 6×10^{-12} erg cm $^{-2}$ s $^{-1}$ at ~ 4 GeV.

The synchrotron self Compton component of the reverse shock peaks (in ϵF_{ϵ}) at $\epsilon_{c,RS}^{SSC} \approx 2\gamma_{c,RS}^2 \epsilon_{c,RS} \approx 35$ keV. The Compton Y parameter, which gives the luminosity ratio of the SSC to the synchrotron component is $Y_{RS}^{SSC} = (-1 + \sqrt{1 + 4\eta_{RS}^{SSC} \epsilon_e / \epsilon_B}) / 2 \approx 0.031$ (Sari & Esin 2001), where $\eta_{RS}^{SSC} = \min((\gamma_c^{RS} / \gamma_m^{RS})^{2-p}, 1)$. In this slow cooling regime, $\eta_{RS}^{SSC} < 1$ is valid. The amplitude of the RS-SSC is obtained from $(\epsilon F_{\epsilon})_{SSC}^{\text{peak}} = Y_{RS}^{SSC} \epsilon_c^{RS} F_{\epsilon_c}^{RS} \approx 3.5 \times 10^{-10}$ erg cm $^{-2}$ s $^{-1}$. While this component can have fluxes of the order of 10^{-8} erg cm $^{-2}$ s $^{-1}$, it is dominated by other components.

The prompt emission will generate an SSC component. The peak energy of this component $2\gamma_{e,ph}^2 \epsilon_{br} \approx 0.2$ TeV falls in the deep KN regime and its ϵF_{ϵ} peak will be less than 10^{-9} erg cm $^{-2}$ s $^{-1}$.

B. Klein-Nishina break for SSC and EIC components

Klein-Nishina effects are potentially important when assessing high-energy, inverse Compton components. In our study we investigate the KN break for SSC and EIC components of both the FS and RS with the prompt emission. We

calculate the KN break energy based on Guetta & Granot (2003b). The KN break occurs at the solution of the $\varepsilon = \gamma_{max}(\varepsilon)m_e c^2$, where γ_{max} is a function of ε (for the detailed expression of $\gamma_{max}(\varepsilon)$ see Guetta & Granot 2003b). Depending on the radiative regime and the position of ε_{KN}^{IC} with respect to the characteristic IC frequencies, we have four cases for each regime (IC here stands for either EIC and SSC emission). In the fast cooling case (valid here for FS-EIC and FS-SSC) we need to solve:

$$\varepsilon_{KN}^{IC} = \begin{cases} (m_e c^2)^2 / \varepsilon'_c & \text{if } \gamma_c^2 \varepsilon'_c < \varepsilon_{KN}^{IC} < \gamma_m^2 \varepsilon'_c \\ m_e c^2 \gamma_m & \text{if } \gamma_m^2 \varepsilon'_c < \varepsilon_{KN}^{IC} < \gamma_m^2 \varepsilon'_m (= \varepsilon_m^{IC}) \\ (m_e c^2)^2 / \varepsilon'_m & \text{if } \gamma_m^2 \varepsilon'_m < \varepsilon_{KN}^{IC} < \gamma_M^2 \varepsilon'_m \\ m_e c^2 \gamma_M & \text{if } \gamma_M^2 \varepsilon'_m < \varepsilon_{KN}^{IC} \end{cases} \quad (\text{B1})$$

for ε_{KN}^{IC} . Above the break the spectrum will change to $F_\varepsilon \propto \varepsilon^{-(p+1-\alpha)}$ or in some cases to $F_\varepsilon \propto \varepsilon^{-(2-\alpha)}$ in the fast cooling, or to $F_\varepsilon \propto \varepsilon^{-(p-\alpha)}$ in slow cooling regime. In the slow cooling regime (used here for RS-SSC and RS-EIC) we can obtain the break energy by swapping the roles of the cooling (c) and characteristic (m) quantities in the above equation.

REFERENCES

- Abdo, A. A. et al. 2009, *Science*, 323, 1688
- Abdo, A. A., & the Fermi collaboration. 2009, *ApJ*, 706, L138, 0909.2470
- Ackermann, M., & the Fermi collaboration. 2011, *ApJ*, 729, 114, 1101.2082
- Ando, S., & Mészáros, P. 2008, *ApJ*, 689, 351, 0808.1722
- Asano, K., Inoue, S., & Mészáros, P. 2010, *ApJ*, 725, L121, 1009.5178
- Band, D. et al. 1993, *ApJ*, 413, 281
- Beloborodov, A. M. 2005, *ApJ*, 618, L13, arXiv:astro-ph/0410050
- . 2010, *MNRAS*, 407, 1033, 0907.0732
- Bošnjak, Ž., & Kumar, P. 2012, *MNRAS*, L390, 1108.0929
- Drenkhahn, G. 2002, *A&A*, 387, 714, arXiv:astro-ph/0112509

- Drenkhahn, G., & Spruit, H. C. 2002, *A&A*, 391, 1141, arXiv:astro-ph/0202387
- Fan, Y., & Piran, T. 2006, *MNRAS*, 370, L24, arXiv:astro-ph/0601619
- Frajia, N., Magdalena Gonzalez, M., & Lee, W. H. 2012, ArXiv e-prints, 1201.3689
- Ghisellini, G., Ghirlanda, G., Nava, L., & Celotti, A. 2009, ArXiv e-prints, 0910.2459
- Giannios, D. 2008, *A&A*, 480, 305, 0711.2632
- . 2012, *MNRAS*, 2865, 1111.4258
- Giannios, D., Mimica, P., & Aloy, M. A. 2008, *A&A*, 478, 747, 0711.1980
- Giannios, D., & Spruit, H. C. 2007, *A&A*, 469, 1, arXiv:astro-ph/0611385
- Guetta, D., & Granot, J. 2003a, *ApJ*, 585, 885, arXiv:astro-ph/0209578
- . 2003b, *MNRAS*, 340, 115, arXiv:astro-ph/0208156
- Guiriec, S. et al. 2011, *ApJ*, 727, L33, 1010.4601
- He, H.-N., Wu, X.-F., Toma, K., Wang, X.-Y., & Mészáros, P. 2011, *ApJ*, 733, 22, 1009.1432
- Kennel, C. F., & Coroniti, F. V. 1984, *ApJ*, 283, 710
- Kocevski, D., & The Fermi Collaboration. 2012, ArXiv e-prints, 1201.3948
- Komissarov, S. S., Vlahakis, N., Königl, A., & Barkov, M. V. 2009, *MNRAS*, 394, 1182, 0811.1467
- Kumar, P., & Barniol Duran, R. 2009, *MNRAS*, 400, L75, 0905.2417
- Lazzati, D., Morsony, B. J., & Begelman, M. C. 2011, *ApJ*, 732, 34, 1101.3788
- Lazzati, D., Rossi, E., Ghisellini, G., & Rees, M. J. 2004, *MNRAS*, 347, L1, arXiv:astro-ph/0309038
- Lithwick, Y., & Sari, R. 2001, *ApJ*, 555, 540, arXiv:astro-ph/0011508
- Lyutikov, M., & Blandford, R. 2003, ArXiv Astrophysics e-prints, arXiv:astro-ph/0312347

- McKinney, J. C., & Uzdensky, D. A. 2011, *MNRAS*, 1766, 1011.1904
- Mészáros, P., & Rees, M. J. 1993, *ApJ*, 418, L59+, arXiv:astro-ph/9309011
- . 1994, *MNRAS*, 269, L41+, arXiv:astro-ph/9404056
- . 1997, *ApJ*, 476, 232, arXiv:astro-ph/9606043
- Mészáros, P., & Rees, M. J. 2011, *ApJ*, 733, L40+, 1104.5025
- Metzger, B. D., Giannios, D., & Horiuchi, S. 2011a, *MNRAS*, 415, 2495, 1101.4019
- Metzger, B. D., Giannios, D., Thompson, T. A., Bucciantini, N., & Quataert, E. 2011b, *MNRAS*, 413, 2031, 1012.0001
- Mimica, P., & Aloy, M. A. 2011, ArXiv e-prints, 1111.3170
- Murase, K., & Ioka, K. 2008, *ApJ*, 676, 1123, 0708.1370
- Murase, K., Toma, K., Yamazaki, R., & Mészáros, P. 2011, *ApJ*, 732, 77, 1011.0988
- Nakar, E., Piran, T., & Waxman, E. 2003, *J. Cosmology Astropart. Phys.*, 10, 5, arXiv:astro-ph/0307290
- Narayan, R., Kumar, P., & Tchekhovskoy, A. 2011, *MNRAS*, 416, 2193, 1105.0003
- Narayan, R., Tchekhovskoy, A., & McKinney, J. 2010, in *Astronomical Society of the Pacific Conference Series*, Vol. 427, *Accretion and Ejection in AGN: a Global View*, ed. L. Maraschi, G. Ghisellini, R. Della Ceca, & F. Tavecchio, 127–+, 1001.1355
- Omodei, N., & the Fermi LAT collaboration. 2011, Talk at Fermi Meeting, Stanford U.
- Page, K. L. et al. 2011, *MNRAS*, 416, 2078
- Pe’er, A. 2011, ArXiv e-prints, 1111.3378
- Pe’er, A., Mészáros, P., & Rees, M. J. 2006, *ApJ*, 642, 995, arXiv:astro-ph/0510114
- Pe’er, A., Zhang, B.-B., Ryde, F., McGlynn, S., Zhang, B., Preece, R. D., & Kouveliotou, C. 2012, *MNRAS*, 420, 468, 1007.2228

- Pelassa, V. 2011, in American Institute of Physics Conference Series, Vol. 1358, American Institute of Physics Conference Series, ed. J. E. McEnery, J. L. Racusin, & N. Gehrels, 41–46
- Racusin, J. L. et al. 2008, *Nature*, 455, 183, 0805.1557
- Rees, M. J., & Mészáros, P. 2005, *ApJ*, 628, 847, arXiv:astro-ph/0412702
- Ryde, F. et al. 2010, *ApJ*, 709, L172, 0911.2025
- Sari, R., & Esin, A. A. 2001, *ApJ*, 548, 787, arXiv:astro-ph/0005253
- Sari, R., & Mészáros, P. 2000, *ApJ*, 535, L33, arXiv:astro-ph/0003406
- Sari, R., Piran, T., & Narayan, R. 1998, *ApJ*, 497, L17+, arXiv:astro-ph/9712005
- Thompson, C. 1994, *MNRAS*, 270, 480
- Toma, K., Sakamoto, T., & Mészáros, P. 2011a, *ApJ*, 731, 127, 1008.1269
- Toma, K., Wu, X.-F., & Mészáros, P. 2011b, *MNRAS*, 415, 1663, 1002.2634
- Vurm, I., Beloborodov, A. M., & Poutanen, J. 2011, *ApJ*, 738, 77, 1104.0394
- Waxman, E. 2003, *Nature*, 423, 388, arXiv:astro-ph/0305414
- Yonetoku, D. et al. 2011, *ApJ*, 743, L30, 1111.1779
- Zhang, B., & Kobayashi, S. 2005, *ApJ*, 628, 315, arXiv:astro-ph/0404140
- Zhang, B., & Yan, H. 2011, *ApJ*, 726, 90, 1011.1197
- Zhang, B.-B. et al. 2011, *ApJ*, 730, 141, 1009.3338
- Zhao, X.-H., Li, Z., & Bai, J.-M. 2011, *ApJ*, 726, 89, 1005.5229
- Zou, Y.-C., Fan, Y.-Z., & Piran, T. 2011, *ApJ*, 726, L2, 1008.2253